Supporting Information

Photochromic Bi_2WO_6/BiOBr ultrathin nanosheet heterojunctions for efficient photocatalytic synthesis of imine via toluene and aniline coupling

Jiazhen Han, Guanfeng Ji, Yao Dou, Yongli Qin, Xin Liu, Yun Zhang*, Wenshou Wang*

School of Chemistry and Chemical Engineering, University of Jinan, Jinan 250022, P.R. China

Corresponding Author: chm_zhangy2022@ujn.edu.cn, chm_wangws@ujn.edu.cn

Materials

Bismuth (III) nitrate pentahydrate ($Bi(NO_3)_3 \cdot 5H_2O$), tetramethylpiperidine (TEMPO, 98.0%), acetonitrile (CH_3CN), p-benzoquinone (BQ, 99.0%), 1,3,5-trimethoxybenzene (AR, 98.0%), and ethylbenzene(C_8H_{10}) were purchased from Shanghai Macklin Chemical Reagent Co., Ltd. Potassium iodide (KI, AR, 99.0%), silver nitrate ($AgNO_3$, AR, 99.8%), sodium tungstate dihydrate ($Na_2WO_4 \cdot 2H_2O$), aniline (C_6H_7N), barium sulfate ($BaSO_4$), cetyltrimethylammonium bromide (CTAB), sodium chloride (NaCl) mannitol, ethyl acetate ($C_4H_8O_2$) and dichloromethane (CH_2Cl_2) were purchased from Sinopharm Chemical Reagent Co., Ltd. Nitric acid (HNO_3, 65-68%), toluene (C_7H_8) from Yantai Far East Fine Chemical Co., Ltd.

Characterization

Powder X-ray diffraction (XRD) patterns were recorded using a Rigaku SmartLab diffractometer equipped with graphite monochromatized Cu Kα radiation (λ = 1.5418 Å). The morphological and structural characterizations were performed using field emission scanning electron microscope (SEM, Zeiss, Gemini 300) and transmission electron microscopy (TEM, Hitachi-7700), equipped with an Energy Dispersive Spectrometer (EDS, Oxford, X-MaxN 50) for elemental composition analysis. X-ray photoelectron spectroscopy (XPS) was performed on a Thermo Scientific ESCALAB 250 Xl and Thermo Fisher ESCALAB Xl^+ spectrometer equipped with an Al Kα X-ray source. Raman spectra of the samples were obtained by a micro-Raman LabRAM HR800 spectrometer (Horiba Jobin Yvon, Japan) with laser excitation at λ = 633 nm. Electron spin resonance (EPR) spectrum was obtained using a EPR100 spectrometer at X-band at 25 ^oC. Low-temperature EPR spectra were acquired on a Bruker EMX PLUS spectrometer at 100 K. The Fourier transform infrared (FT-IR) spectra were acquired on a Bruker VERTEX 70 in the range of 400-2000 cm^{-1}. Ultraviolet-visible (UV-vis) diffuse reflectance spectra were acquired in the spectral region of 200-800 nm with a Thermo UV-2600 spectrophotometer, using $BaSO_4$ as

reference. Photoluminescence (PL) spectra of the samples were collected on a Shimadzu HRF-6000 spectrometer with excitation wavelengths of 320 nm. The thickness of the samples was measured by atomic force microscopy (AFM, Dimension Icon) on mica substrates.

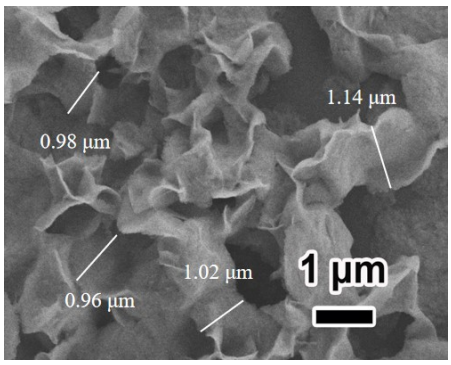

Fig. S1 SEM image of Bi_2WO_6/BiOBr UNHs showing a size of approximately 1.00 μm.

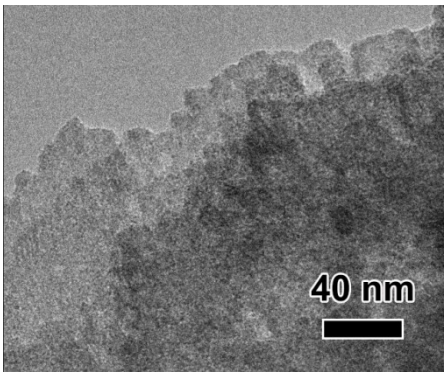

Fig. S2 TEM image of Bi_2WO_6/BiOBr UNHs.

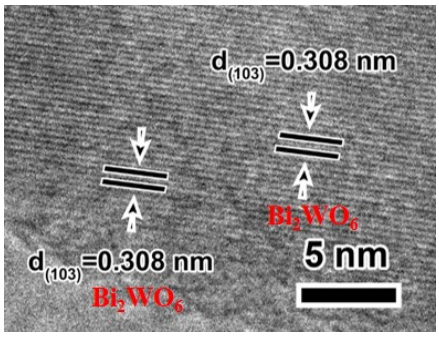

Fig. S3 HRTEM image of Bi_2WO_6/BiOBr UNHs in other regions.

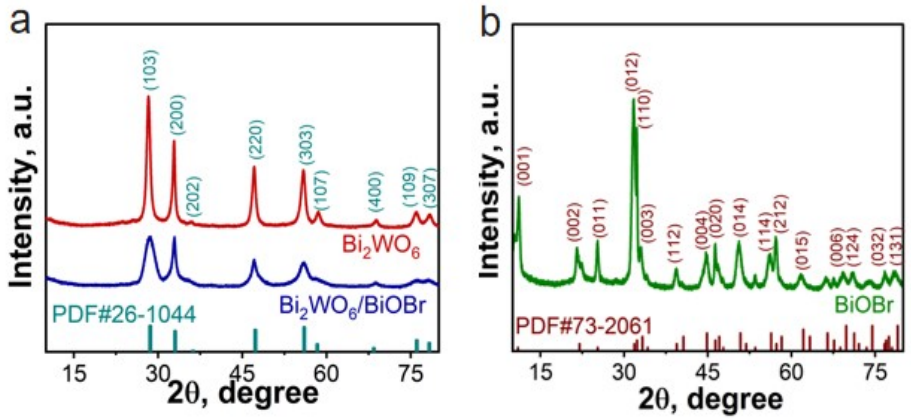

Fig. S4 The XRD patterns of Bi_2WO_6 and Bi_2WO_6/BiOBr UNHs (a), BiOBr after nitric acid treatment (b).

XRD analysis further confirmed the biphasic composition of the heterojunction sample, consisting of crystalline Bi_2WO_6 and BiOBr phases (Fig. S3). The XRD pattern of the Bi_2WO_6/BiOBr UNHs displays a similar diffraction peak with that of pure Bi_2WO_6 (JCPDS 26-1044). However, the diffraction peaks of heterojunctions are significantly broadened, which indicates the formation of ultrathin nanosheets. As comparison with pure BiOBr (JCPDS No. 73-2061), the diffraction peaks related to BiOBr in the heterojunctions is inapparent, which might be related to that the diffraction peaks of (012), (110), and (003) crystal planes of BiOBr are overlapped with the (200) crystal plane of Bi_2WO_6, and the content of BiOBr in the heterojunction is low (about 13%, Fig. 1e) leading to weak diffraction intensity.

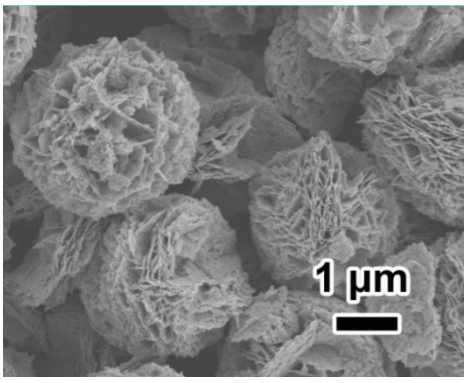

Fig. S5 SEM image of Bi_2WO_6.

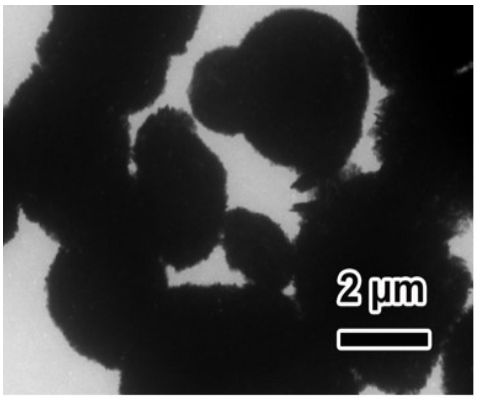

Fig. S6 TEM image of Bi_2WO_6.

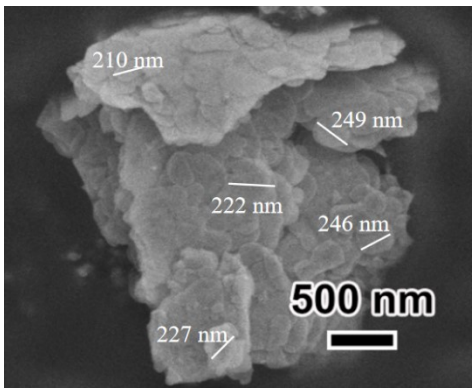

Fig. S7 SEM image of BiOBr reveals a size of approximately 210 to 250 nm.

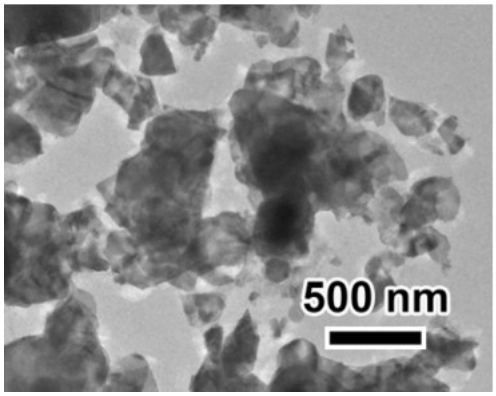

Fig. S8 TEM image of BiOBr.

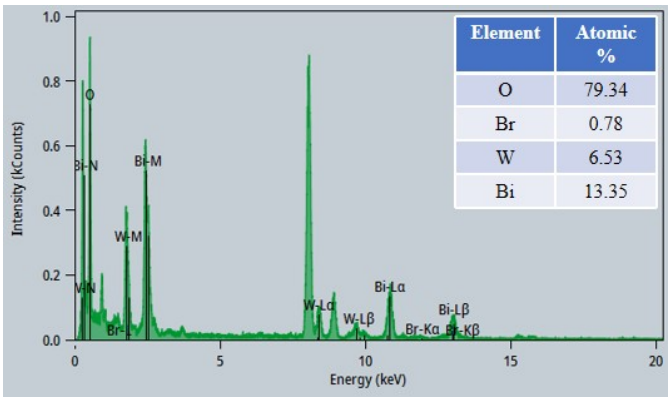

Fig. S9 The EDS spectrum of typical Bi_2WO_6/BiOBr UNHs.

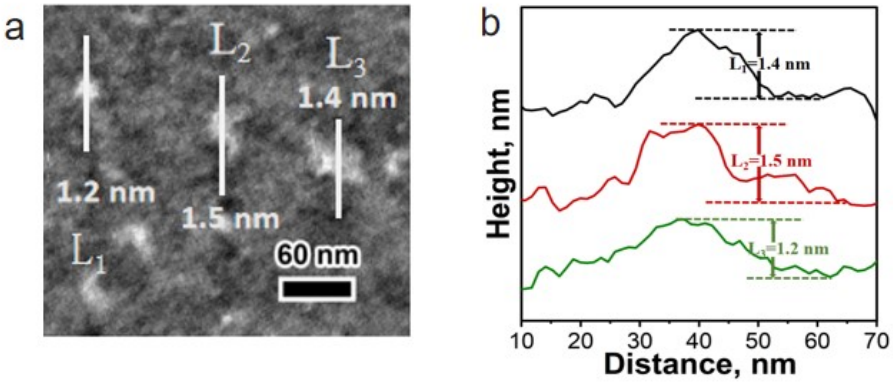

Fig. S10 AFM image (a) and corresponding height profiles (b) of Bi_2WO_6/BiOBr UNHs.

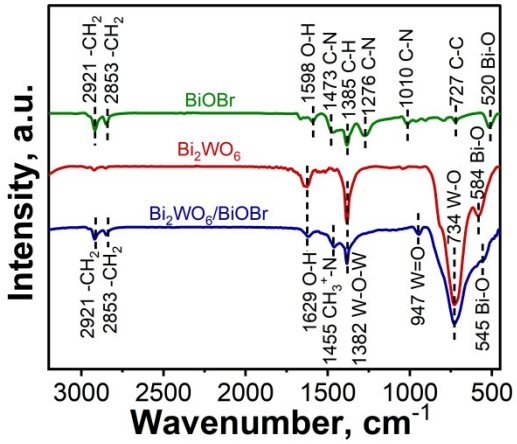

Fig. S11 FT-IR spectra of BiOBr, Bi_2WO_6, and Bi_2WO_6/BiOBr UNHs.

For BiOBr, the peaks located at 727, 1010, 1276, 1385, 1473, 2853, and 2921 cm^{-1}, are attributed to the organic groups from CTAB. Specifically, the peaks at 2853 and 2921 cm^{-1} are assigned to the C-H stretching modes, while those at 1010, 1276,

and 1473 cm^{-1} correspond to C-N stretching vibrations. The peak at 727 cm^{-1} is characteristic of C-C bonds. Furthermore, the spectra exhibited peaks at 1598 and 1629 cm^{-1}, which are attributed to O-H stretching vibrations of adsorbed water.

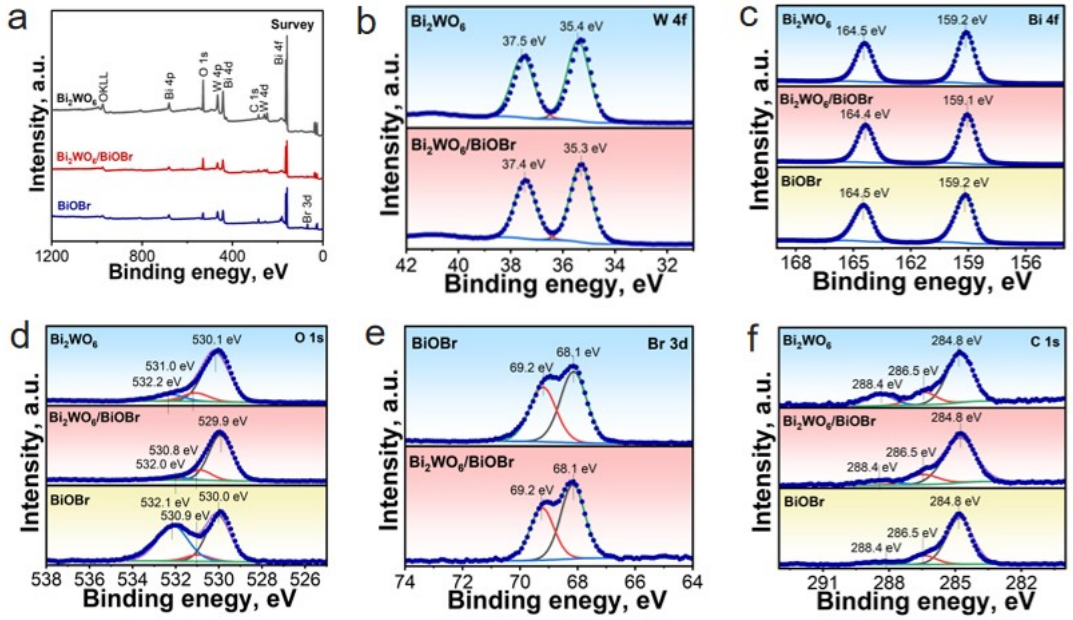

Fig. S12 (a-f) The XPS survey (a), high-resolution XPS spectra of W 4f (b) , Bi 4f (c), O 1s (d), Br 3d (e), and C 1s (f) of BiOBr, Bi_2WO_6, and Bi_2WO_6/BiOBr UNHs.

The XPS survey of Bi_2WO_6/BiOBr UNHs revealed element exists of Br, W, Bi and O, which verified the simultaneous presence of Bi_2WO_6 and BiOBr (Fig. S12a). Fig. S12d presents the O 1s spectrum of Bi_2WO_6/BiOBr UNHs, with peaks at 529.9, 530.8, and 532.0 eV attributable to lattice oxygen (Bi-O), oxygen vacancies, and surface-adsorbed oxygen species, respectively[S1]. Compared to pure Bi_2WO_6 and BiOBr, O 1s XPS peak of Bi_2WO_6/BiOBr UNHs was shifted to low binding energy about 0.1 eV. The Br 3d XPS spectra of both BiOBr and Bi_2WO_6/BiOBr UNHs display peaks at 68.1 and 69.2 eV, corresponding to Br $3d_{5/2}$ and Br $3d_{3/2}$ electrons (Fig. S12e)[S2]. As a reference, the C 1s spectra exhibited three characteristic peaks at 284.8, 286.5, and 288.4 eV, which are assigned to the C=C, C–C/C–O/C–N, and O–C=O functional groups, respectively (Fig. S12f)[S3]. The above results demonstrate that Bi_2WO_6/BiOBr UNHs were successfully constructed with strong interfacial interaction.

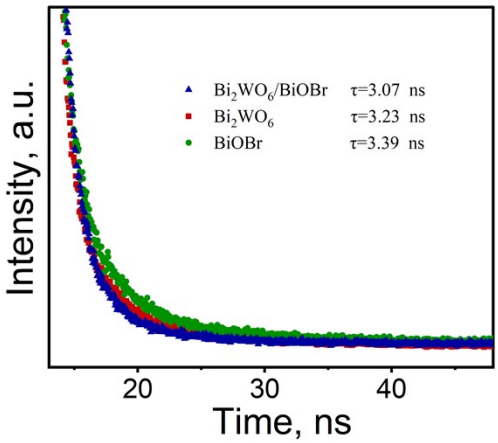

Fig.S13 Time-resolved photoluminescence (TR-PL) decay spectra of BiOBr, Bi_2WO_6, and Bi_2WO_6/BiOBr UNHs.

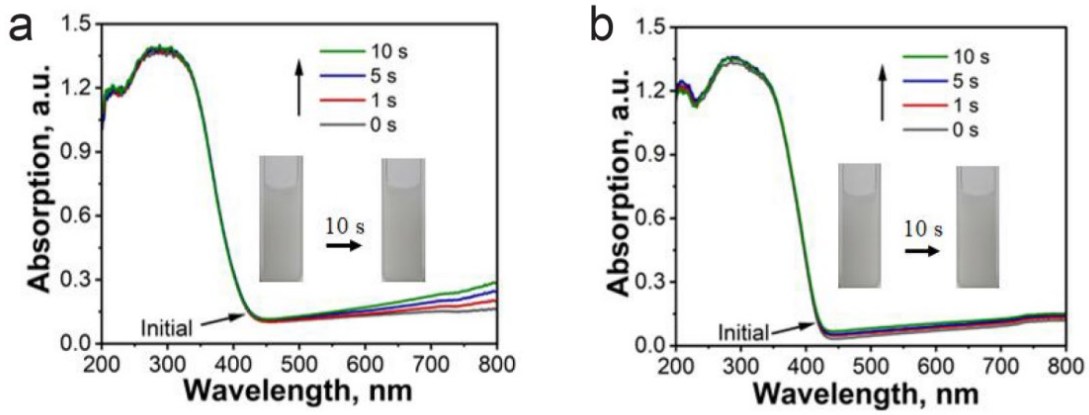

Fig. S14 UV-vis diffuse reflectance spectra showing the coloration process of Bi_2WO_6 (a) and BiOBr (b) in water. Inset in (a, b) are the corresponding digital photographs.

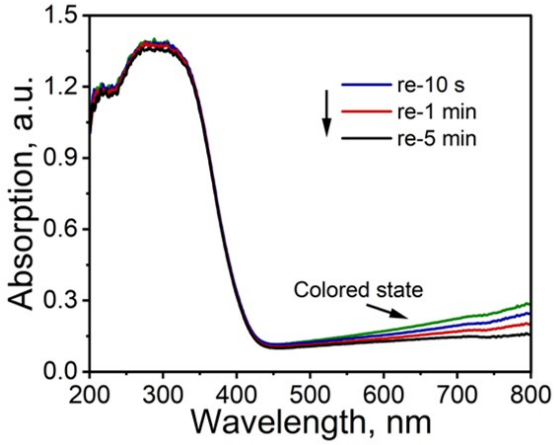

Fig. S15 UV-vis diffuse reflectance spectra showing the decoloration process of

Bi_2WO_6 in water in ambient condition.

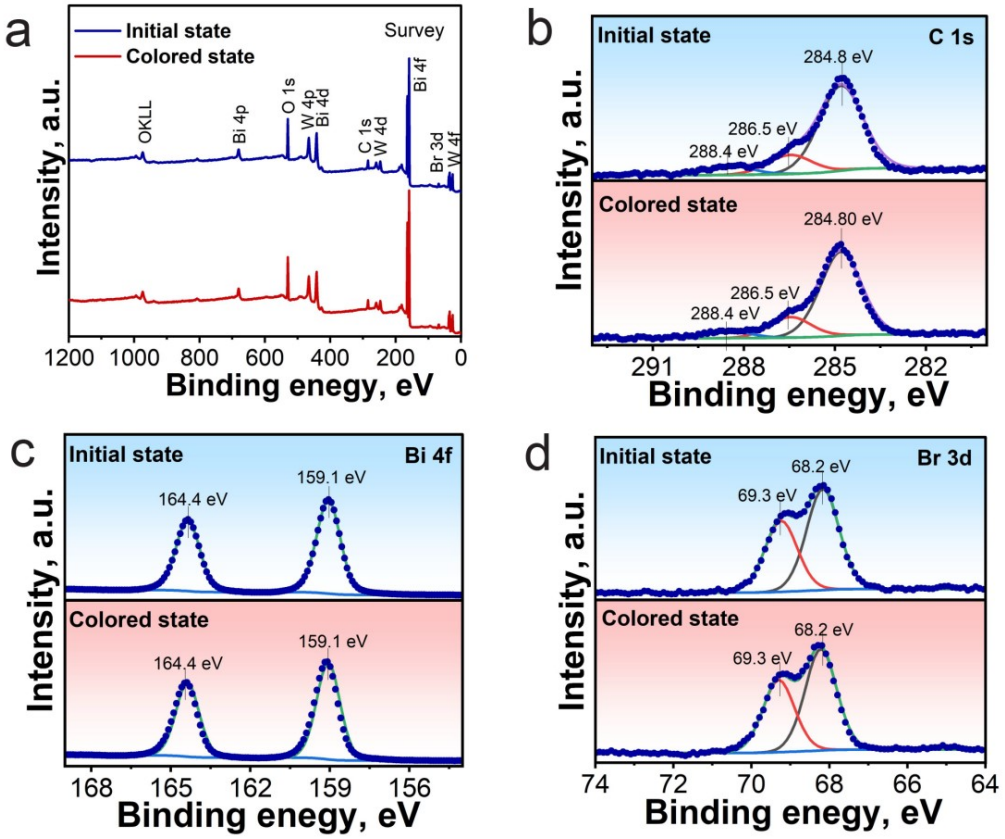

Fig. S16 (a-d) The XPS survey (a), high-resolution XPS spectra of C 1s (b), Bi 4f (c), and Br (d) of Bi_2WO_6/BiOBr UNHs before and after 420 nm light irradiation.

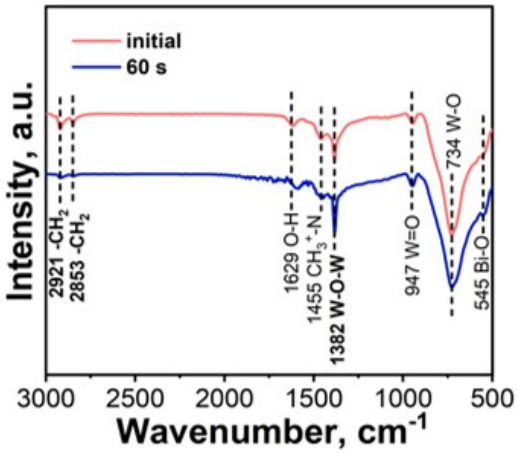

Fig. S17 FI-IR spectra of Bi_2WO_6/BiOBr UNHs before and after 420 nm light irradiation.

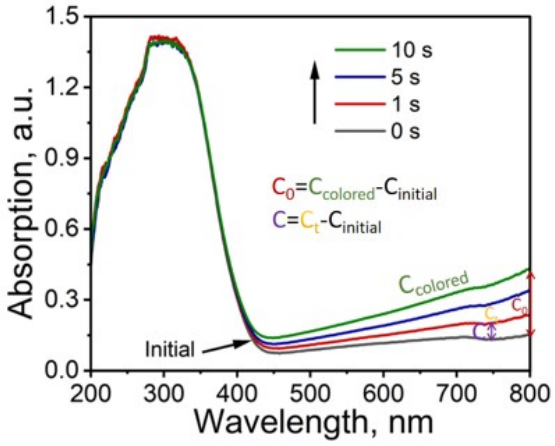

Fig. S18 Schematic illustration of the calculating of C_0 and C for BiOBr, Bi_2WO_6, and Bi_2WO_6/BiOBr UNHs in water. $C_{initial}$ and $C_{colored}$ represent the absorption intensity of the colorless initial aqueous dispersion (800 nm) and the absorption intensity of the colored state (800 nm) upon 420 nm light irradiation for 10 s, respectively. C_t represents the absorption intensity of the aqueous dispersion in various states at a certain time under 420 nm light irradiation during coloration process. C and C_0 are defined as $C = C_t - C_{initial}$ and $C_0 = C_{colored} - C_{initial}$. Then, C/C_0 was used to describe the coloration rate of aqueous dispersion.

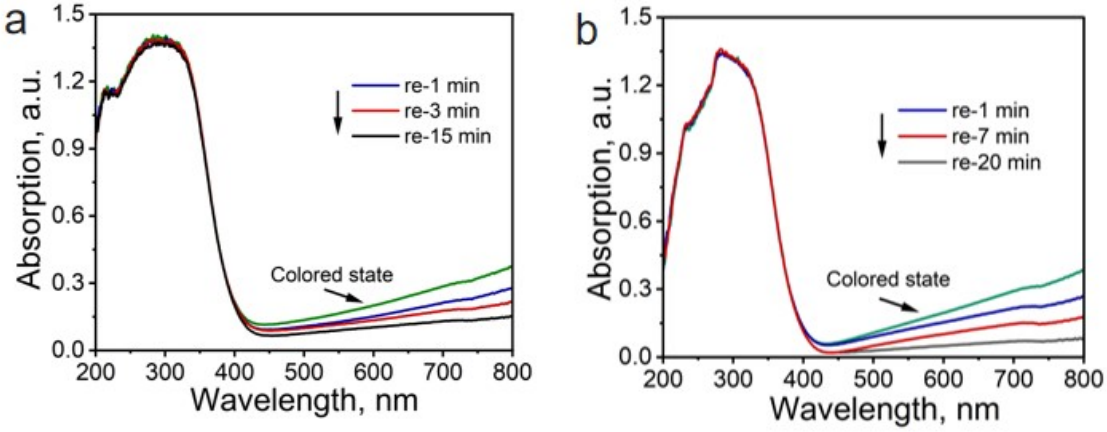

Fig. S19 (a-b) UV-vis diffuse reflectance spectra showing the decoloration process of Bi_2WO_6/BiOBr UNHs in water (a) and mixed solvent of ethylbenzene: acetonitrile (1:1) (b) in ambient condition.

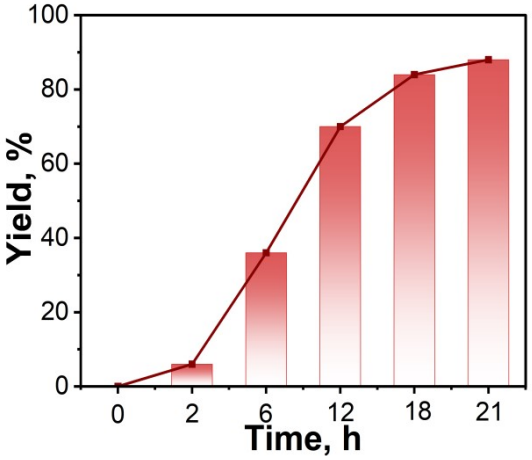

Fig. S20 Time tracking of the ethylbenzene oxidation experiment.

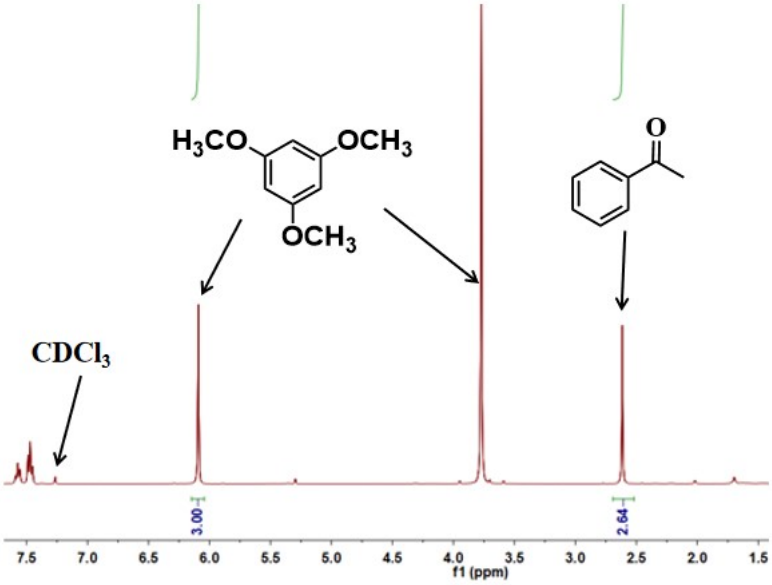

Fig. S21 ^{1}H NMR of acetophenone under standard condition. Standard condition: 298 K, oxygen, 0.1 mmol ethylbenzene, 3 mL MeCN, 10 mg Bi_2WO_6/BiOBr UNHs catalyst, 420 nm (100 W) LED light, 21 h (0.1 mmol 1,3,5-trimethoxybenzene as internal standard).

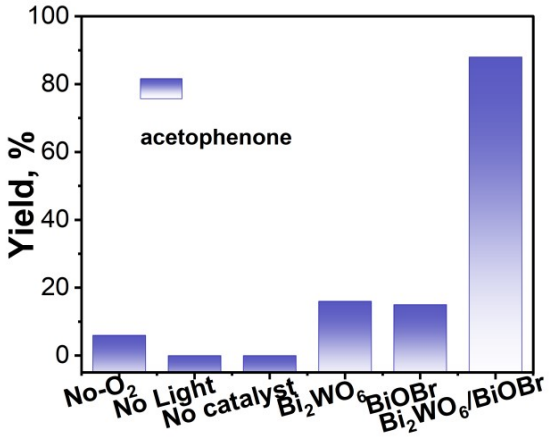

Fig. S22 Photocatalytic oxidation of ethylbenzene under different conditions.

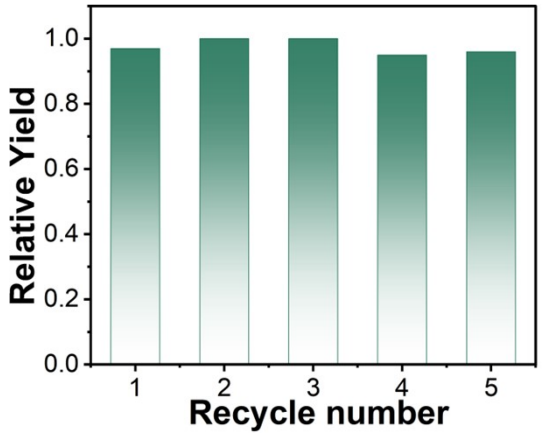

Fig. S23 Cycle experiment of photocatalytic oxidation of ethylbenzene over Bi_2WO_6/BiOBr UNHs.

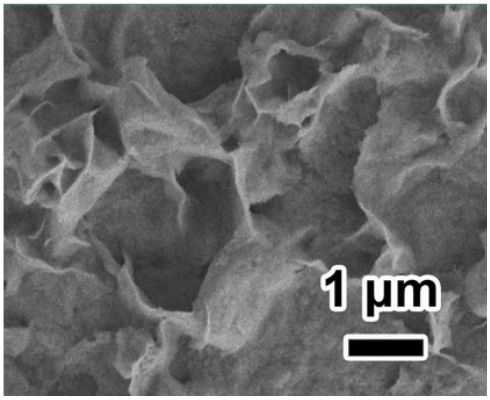

Fig. S24 The SEM image of Bi_2WO_6/BiOBr UNHs after reaction.

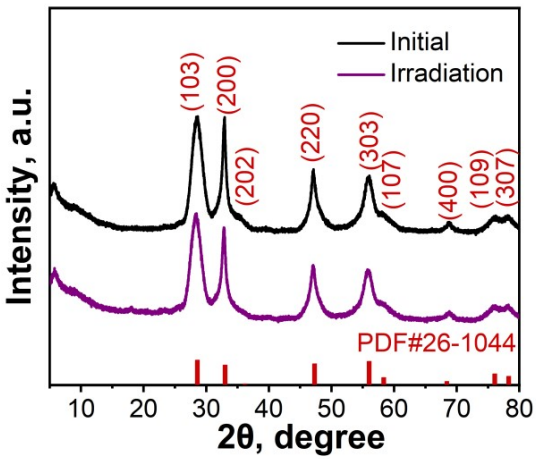

Fig. S25 The XRD spectra of Bi_2WO_6/BiOBr UNHs before and after reaction.

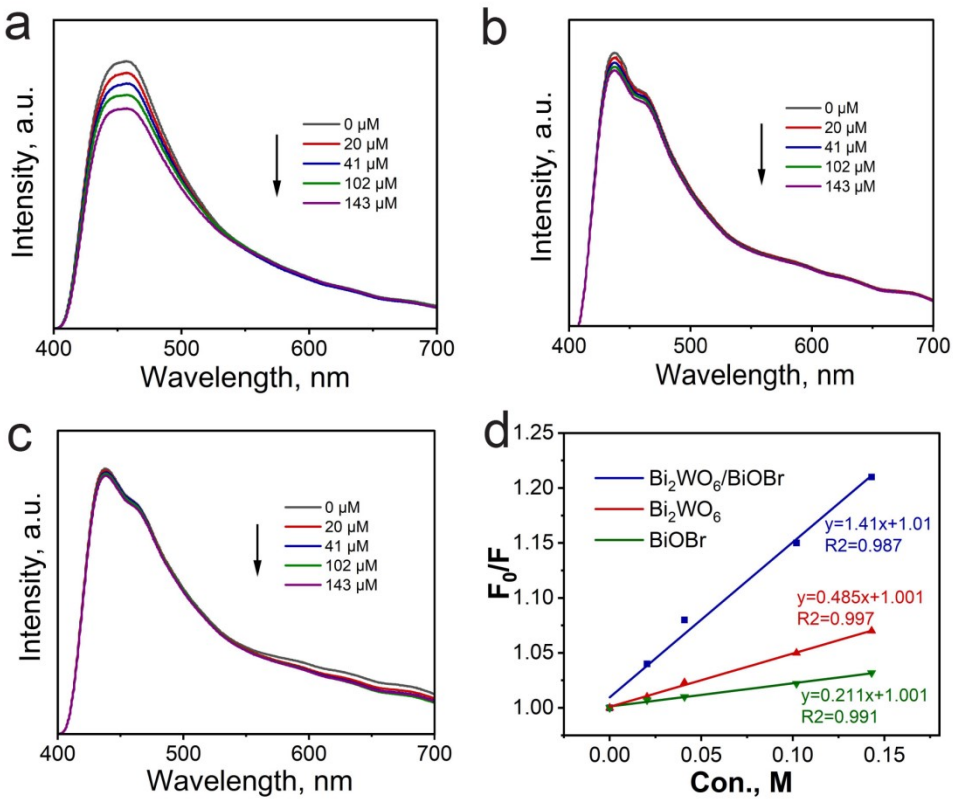

Fig. S26 (a-c) Emission spectra of Bi_2WO_6/BiOBr UNHs (a), Bi_2WO_6 (b), and BiOBr (c) at different concentrations of ethylbenzene, (d) Stern-Volmer plot of Bi_2WO_6, BiOBr, and Bi_2WO_6/BiOBr UNHs at different concentrations of ethylbenzene.

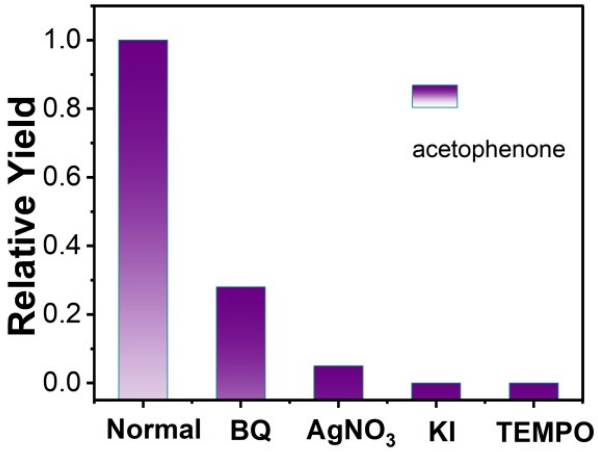

Fig. S27 Relationship between the yield of the oxidative reaction and additives.

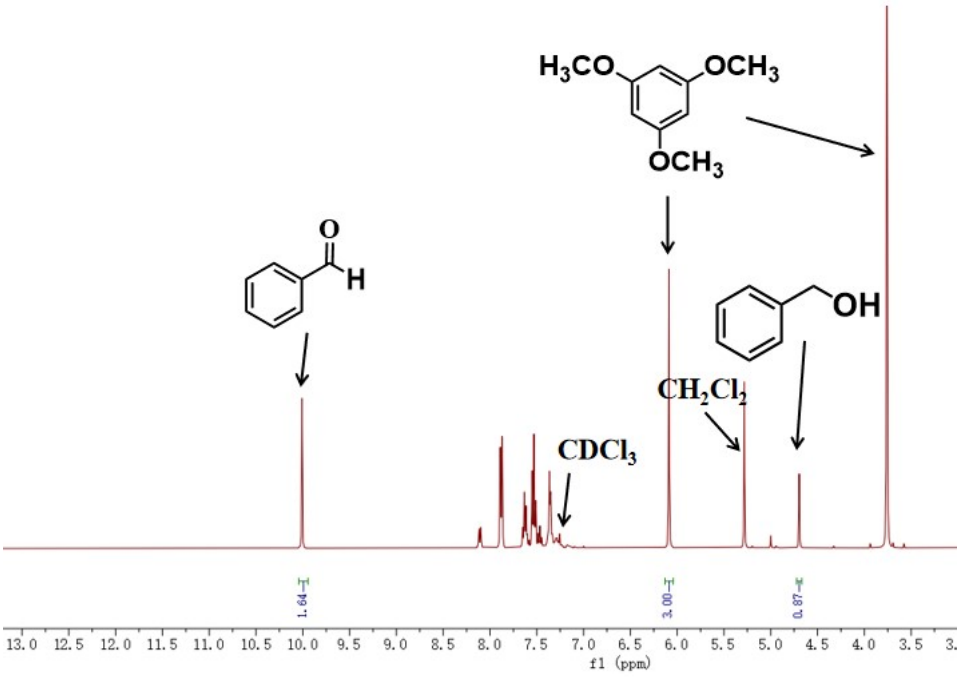

Fig. S28 ^{1}H NMR of benzaldehyde from the photocatalytic oxidation of toluene under standard condition. Standard condition: 298 K, 1 mL toluene, 2 mL MeCN, 10 mg Bi_2WO_6/BiOBr UNHs, 405 nm (100 W) LED light, 2 h (0.1 mmol 1,3,5-trimethoxybenzene as internal standard). The toluene was evaporated during the rotary evaporation process in the preparation of the ^{1}H NMR sample.

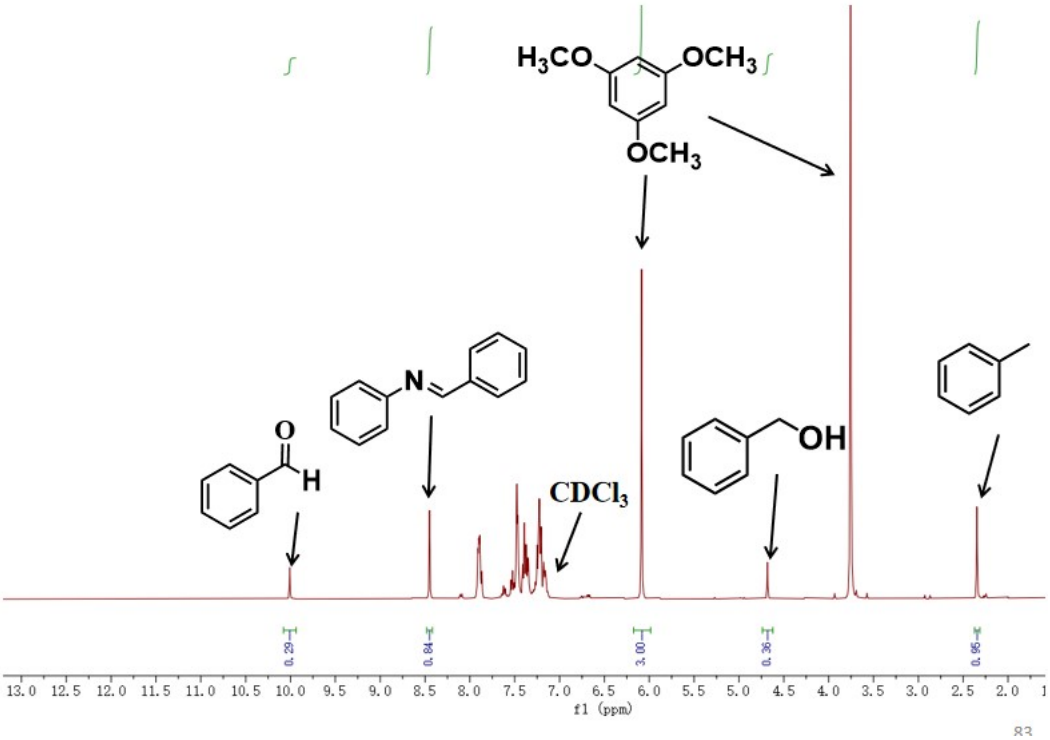

Fig. S29 ^{1}H NMR of imines from the photocatalytic oxidation of toluene coupled with aniline under standard condition. Standard condition: 298 K, 1 mL toluene (2 h), 0.1 mmol aniline (2 h), 2 mL MeCN, 10 mg Bi_2WO_6/BiOBr UNHs, 405 nm (100 W) LED light. The yield was determined by ^{1}H NMR spectroscopy using 0.1 mmol 1,3,5-trimethoxybenzene as an internal standard.

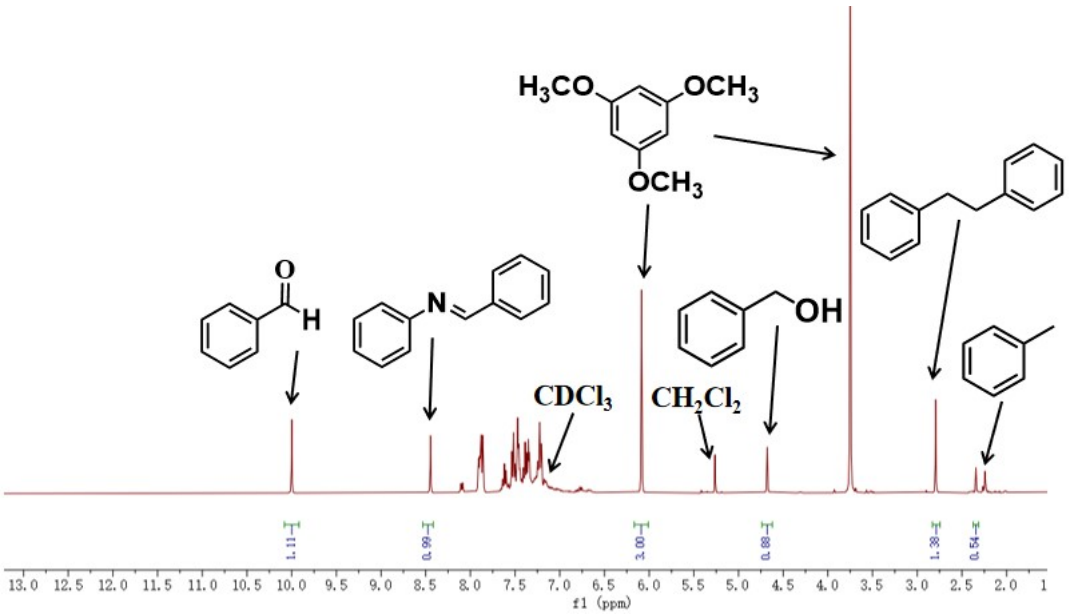

Fig. S30 ^{1}H NMR of imines from the photocatalytic oxidation of toluene coupled with aniline under standard condition. Standard condition: 298 K, 1 mL toluene (2 h), 0.1 mmol aniline (4 h), 2 mL MeCN, 10 mg Bi_2WO_6/BiOBr UNHs, 405 nm (100 W)

LED light. The yield was determined by ^{1}H NMR spectroscopy using 0.1 mmol 1,3,5-trimethoxybenzene as an internal standard.

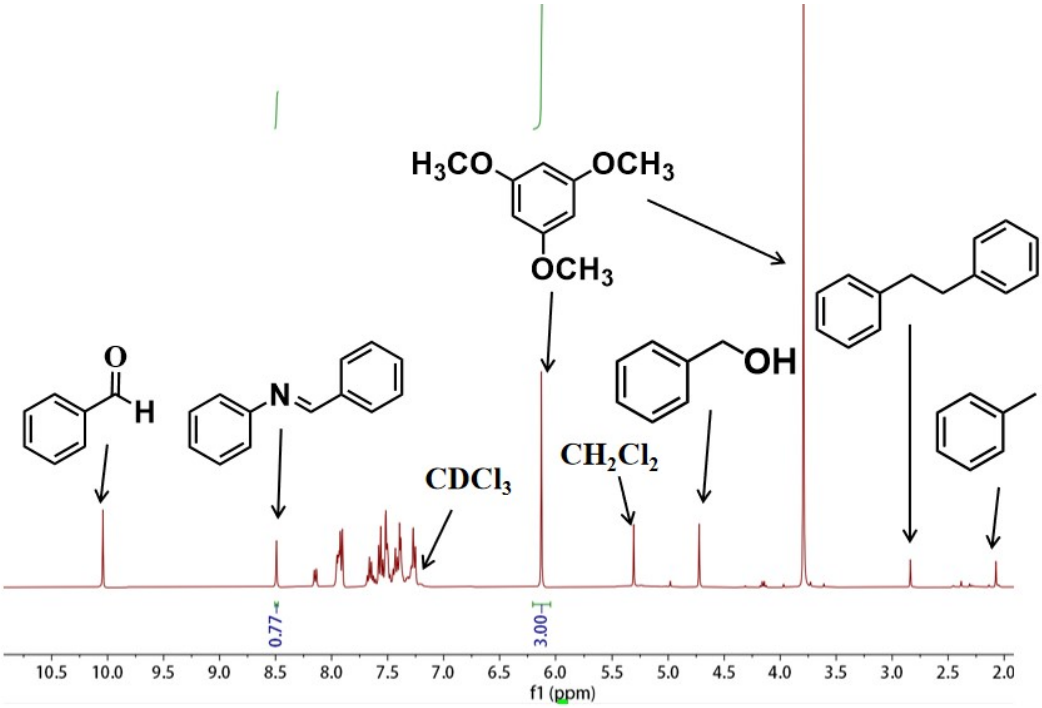

Fig. S31 ^{1}H NMR of imines from the photocatalytic oxidation of toluene coupled with aniline (in the absence of light, in the process of amine condensation reaction).

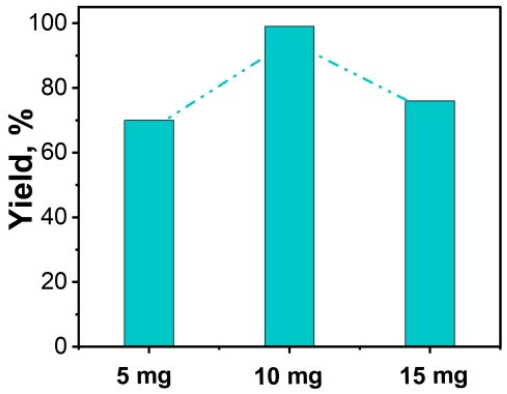

Fig. S32 Photocatalytic performance of coupling toluene with aniline with different amount of photocatalyst in a mixed solvents of 2 ml of acetonitrile and 1 ml of toluene.

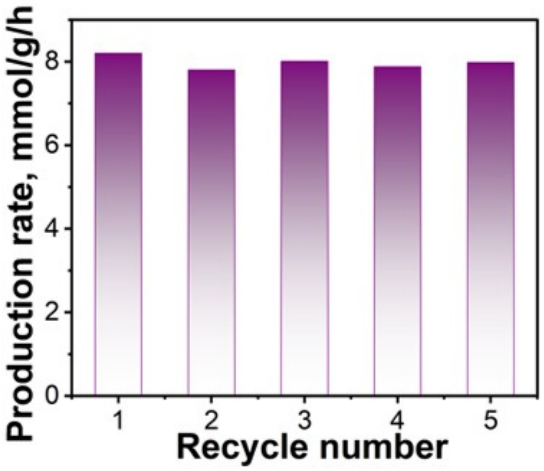

Fig. S33 Cycling experiment of photocatalytic oxidation of toluene over Bi_2WO_6/BiOBr UNHs.

Table S1. Comparison of the photocatalytic aerobic oxidation of ethylbenzene activities of the reported heterogeneous materials

Catalyst	Catalyst amount (mg)	Oxidant	Time (h)	Substrate	Power (w)	Wavelength or Temperature	Yield	Ref.
$BiOBr_{0.98}I_{0.02}$	10	O_2	15	30 mmol	100	450 nm	9.1 %	S4
W-TiO_2	10	O_2	10	3 mL	100	437 nm	8.6 %	S5
TiO_2-PEG200	10	O_2	6	3 mL	100	405 nm	13.8 %	53
Br-CN	180	O_2	24	20 mmol	300	λ > 420 nm	29 %	S6
0.27% PdO/C–Nb_2O_5	100	O_2	12	20 mmol	10	400-405 nm	65.8 %	S7
BBI -0.85	10	O_2	5	0.1 mmol	8	455 nm	81 %	S8
p-BiOBr	20	$C_4H_{10}O$	10	0.2 mmol	300	xenon lamp	93 %	S9
VO@g-C_3N_4	25	H_2O_2	24	1 mmol	40	bulb	99 %	S10
$Ce_{0.5}Mn_{0.5}O_x$	30	O_2	6	1 mmol		120 ℃	18 %	S11
Ce_1/NC	10	O_2	48	0.1 mmol		45 ℃	80 %	S12
This work	10	O_2	21	0.1 mmol	100	420 nm	88 %	

Supplementary references

[S1] X. Kong, W. Lee, A. Mohamed, S. Chai, Effective steering of charge flow through synergistic inducing oxygen vacancy defects and P-N heterojunctions in 2D/2D surface-engineered Bi_2WO_6/BiOI cascade: Towards superior photocatalytic CO_2 reduction activity, Chem. Eng. J. 372 (2019) 1183-1193.

[S2] Y. Zhang, Y. Li, Y. Yuan, Carbon quantum dot-decorated BiOBr/Bi_2WO_6 photocatalytic micromotor for environmental remediation and DFT calculation, ACS Catal. 12 (22) (2022) 13897-13909.

[S3] X. Zhang, Y. Zhang, Z. Feng, J. Zhao, Z. Yang, X. Wang, W. Wang, Self-accelerating photocharge separation in BiOBr ultrathin nanosheets for boosting photoreversible color switching, Chem. Eng. J. 428 (2022) 131235.

[S4] Y. Shan, C. Han, X. Wang, Z. Zhang, M. Yan, G. Ji, W. Wang, Photochromic-activity relationship insights for boosting C(sp^3)-H bonds activation in the $BiOBr_{1-x}I_x$ colloid ultrathin nanosheets, Surf. Interfaces. 72 (2025) 106965.

[S5] Z. Zhang, Y. Zhang, C. Han, M. Yan, G. Ji, W. Wang, Efficient photo-oxidation of C(sp^3)-H bonds on visible-light-responsive W-doped TiO_2 nanocrystals promoted by the photochromic effect, Inorg. Chem. Front. 12 (15) (2025) 4720-4730.

[S6] H. Zhu, J. Zhao, C. Ma, Z. Yu, J. Li, Q. Meng, Bridging effect of carbon nitride with more negative conduction potential and halogens promotes the liquid-phase oxidation of aromatic C-H bonds, ACS Appl. Mater. Interfaces. 15 (51) (2023) 59280-59295.

[S7] X. Jiang, W. Wang, H. Wang, Z. He, Y. Yang, K. Wang, Z. Liu, B. Han, Solvent-free aerobic photocatalytic oxidation of C(sp^3)-H and C(sp^3)-OH to C=O bonds, Green Chem. 26 (8) (2024) 4552-4562.

[S8] Y. Bian, Y. Gu, X. Zhang, H. Chen, Z. Li, Engineering $BiOBr_{1-x}I_x$ solid solutions with enhanced singlet oxygen production for photocatalytic benzylic C-H bond activation mediated by N-hydroxyl compounds, Chin. Chem. Lett. 32 (9) (2021) 2837-2840.

[S9] X. Cao, A. Huang, C. Liang, H. Chen, T. Han, R. Lin, Q. Peng, Z. Zhuang, R. Shen, H. Chen, Y. Yu, C. Chen, Y. Li, Engineering lattice disorder on a photocatalyst: photochromic BiOBr nanosheets enhance activation of aromatic C-H bonds via water oxidation, J. Am. Chem. Soc. 144

(8) (2022) 3386-3397.

[S10] S. Verma, R. Baig, M. Nadagouda, R. Varma, Photocatalytic C-H activation of hydrocarbons over VO@g-C_3N_4, ACS Sustainable Chem. Eng. 4 (4) (2016) 2333-2336.

[S11] P. Zhang, H. Lu, Y. Zhou, L. Zhang, Z. Wu, S. Yang, H. Shi, Q. Zhu, Y. Chen, S. Dai, Mesoporous $MnCeO_x$ solid solutions for low temperature and selective oxidation of hydrocarbons, Nat. Commun. 6 (2015) 8446.

[S12] X. Zhang, Y. Zhong, H. Chen, Y. Cheng, Q. Sun, H. Zhang, Q. He, Y. Zhang, G. Guo, X. He, H. Ji, Synthesis of nitrogen-doped carbon supported cerium single atom catalyst by ball milling for selective oxidation of ethylbenzene, Chem. Res. Chin. Univ. 38 (5) (2022) 1258-1262.